# Oxygen vacancy induced surface stabilization: (110) terminated magnetite

B. Walls,[1,*] O. Lübben,[1] K. Palotás,[2,3] K. Fleischer,[1] K. Walshe,[1] and I. V. Shvets[1]

[1] *School of Physics and Centre for Research on Adaptive Nanostructures and Nanodevices (CRANN), Trinity College Dublin, Dublin 2, Ireland*
[2] *Department of Theoretical Physics, Budapest University of Technology and Economics, Budafoki út 8, H-1111 Budapest, Hungary*
[3] *Institute of Physics, Slovak Academy of Sciences, SK-84511 Bratislava, Slovakia*

Scanning tunneling microscopy (STM) measurements of the (110) surface of magnetite showed the coexistence of two reconstructions: the known $(1 \times 3)$ row reconstruction and a surprising atomic structure of high complexity which occupies a small fraction of the surface. Oxygen vacancies on the $Fe_3O_4$(110) B-terminated surface have previously been determined to be the most energetically favourable surface termination of those considered [Li *et al.*, Surf. Sci. 601, **876** (2007)]. However, this study only investigated oxygen vacancies which were three-fold coordinated. Here, first principle calculations indicate that two-fold coordinated oxygen represents the most energetically stable oxygen vacancy on the B-terminated (110) surface of magnetite. STM simulations reveal that the structure that occupies a small fraction of the surface corresponds to this energetically favourable B-terminated $Fe_3O_4$(110) surface. The oxygen vacancies form an ordered array: along the $[\bar{1}10]$ direction, every second two-fold coordinated oxygen atom is vacant, vacancies are separated by 6 Å. In adjacent two-fold coordinated oxygen rows, the vacancies are shifted in the $[\bar{1}10]$ direction by 3 Å. Density functional theory (DFT) calculations of the spin density distributions indicate that surface and sub-surface octahedrally coordinated iron atoms are charge ordered. The charge ordering and existence of oxygen vacancies act to reduce the surface charge. However, other polarity compensation mechanisms may be at play to stabilize the surface.

PACS numbers: 68.37.Ef, 68.47.Gh, 61.66.-f, 71.15.Mb

## I. INTRODUCTION

Transition metal oxides (TMO) form a diverse range of crystal structures resulting in them exhibiting a wide variety of properties such as: superconductivity [1], semi conductivity [2], magneto resistance [3] as well as acting as some of the best insulators. Magnetite ($Fe_3O_4$) is a half metallic conductor [4, 5], and a high Curie temperature (838 K) ferrimagnet, it furthermore undergoes a metal insulator transition (Verwey transition) at around 120 K [6, 7]. The (001) and (111) surfaces of $Fe_3O_4$ provide catalytic support and act as catalysts in several different reactions including hydrogenation [8] and water dissociation [9–11]. Furthermore, the spin filtering effect at the magnetite-semiconductor interface leads to polarized spin injection [12]. Due to these potential applications, the material's properties and the continued debate over the nature of the Verwey transition [13–18], magnetite has and is still seeing substantial research interest.

$Fe_3O_4$ exists in an inverse spinel crystal structure. The oxygen anions form an FCC sublattice within the unit cell. Fe atoms occupy octahedral ($Fe_{oct}$) or tetrahedral ($Fe_{tet}$) coordinates. $Fe_{oct}$ sites are trivalent or divalent while $Fe_{tet}$ sites are trivalent. At room temperature the conductivity of magnetite arises from the continuous hopping of delocalized electrons between the divalent and trivalent $Fe_{oct}$ sites [19, 20]. Divalent ($3d^6$) and trivalent ($3d^5$) iron atoms have magnetic moments of $4\,\mu_B$ and $5\,\mu_B$, respectively. The antiferromagnetic alignment of octahedral and tetrahedral sites leads to a cancellation of the trivalent magnetic moments. Therefore, magnetite has a magnetic moment of $4\,\mu_B$ per formula unit. (110) terminated magnetite consists of two alternating planes separated by 1.484 Å, namely the A- and B-plane which are illustrated in Fig. 1. The oxygen atoms in each plane form consecutive (110) planes of the oxygen FCC sublattice. The A-plane contains both coordinations of iron while the B-plane only contains $Fe_{oct}$ iron.

The distribution of electrons throughout the unit cell and a relatively complex crystal structure of magnetite lead to all three low index magnetite surfaces, (001), (110) and (111), being polar. (110) terminated magnetite's polarity arises from the unit cells of the A- and B-planes having a charge deficit and excess of $3\,e^-$. Two adjacent planes can therefore be considered as a capacitor, the sequence of capacitors leads to a diverging electrostatic energy [21]. A compensated polar surface is one which avoids this diverging electrostatic energy, it achieves this by reducing its surface charge to zero [22]. Several polarity compensation mechanisms can stabilize polar oxide surfaces: presence of vacancies [23–25], adsorption of foreign species [26], charge redistribution [27], increased surface covalent character [28, 29] or faceting [24]. In some cases, the combination of multiple mechanisms has been observed to stabilize oxide surfaces [24, 25].

STM studies of transition metal oxide surfaces have revealed complex and varying reconstructions: missing oxygen chains lead to a row reconstructed $MoO_2$(100) surface [30], onefold oxygen caps the subsurface layer

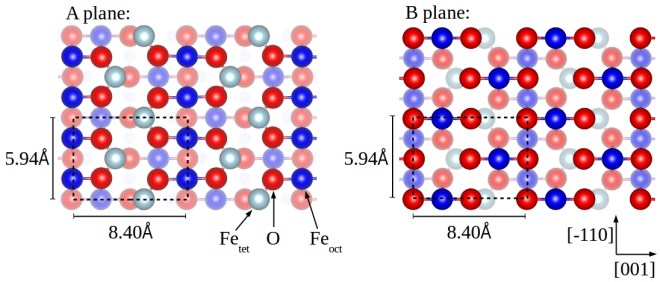


FIG. 1. The A- and B-planes of (110) terminated magnetite. The A-plane contains oxygen and both coordinations of iron, while the B-plane contains oxygen and octahedral iron. The surface unit cells are illustrated by the black dashed rectangles.

which contains rows of missing atoms on the $(2\times1)$ reconstructed $TiO_2(110)$ surface [31] and nanosized triangular and hexagonal islands stabilise the (0001) and $(000\bar{1})$ surfaces of ZnO, respectively [32]. The (001) and (111) surfaces of magnetite also demonstrate complex reconstructions. The (001) - $(\sqrt{2}\times\sqrt{2})$R45° reconstruction is stabilised by subsurface iron vacancies and interstitial surface iron atoms [33]. Three of the six (111) terminations have been observed experimentally, the preparation procedure plays a pivotal role in the termination present. $Fe_{oct}$ [34], $Fe_{tet}$ [35] and oxygen [36] terminated surfaces have been observed, the existence of a combination of these terminations is possible [34, 37]. Surface vacancies are present on all of the terminations with the only exception being the oxygen terminated strain induced superstructure [36]. Theoretical calculations indicate that (111) surfaces containing adatoms or surface vacancies show comparable surface stabilities to their bulk truncated counterparts [38]. Therefore, considering that the (111) surface is magnetite's predominant cleaving plane, one would expect (110) truncated magnetite to also exhibit complex reconstructions.

STM studies on both single crystalline and thin film $Fe_3O_4(110)$ have revealed a $(1\times3)$ row reconstruction [39–45]. However, differences in the number of rows within the unit cell have been reported. Recently the row structure observed by Parkinson *et al.* has been explained as periodic nanofaceting which exposes {111}-type planes [45]. STM measurements in our study not just reveal a row reconstructed surface, but also introduce areas with a surprising atomically flat structure. The coexistence of two different reconstructions on the same surface illustrates that there are several possible terminations with only moderate differences in formation energies. Therefore, this work reveals an added level of complexity to (110) terminated magnetite. The combination of a DFT study of the (110) surface with the simulation of STM images allows us to draw conclusions about the atomically flat surface structure.

## II. EXPERIMENTAL DETAILS

The sample studied in this work was a single crystal which was float zone grown (Moscow State Steel and Alloys Institute). The crystal was initially polished using P2500 grade sandpaper. Subsequently, diamond and cerium oxide suspensions with a final grain size of 0.01 $\mu m$ were used for further polishing until an optically flat surface was achieved [46]. The Verwey transition temperature ($T_V$) was found to be $(122\pm1)$ K [46]. Stoichiometric magnetite is expected to have a $T_V$ of around 120 K [47]. As magnetite becomes cation deficient $T_V$ decreases, and the transition eventually disappears. The Verwey transition has been observed to disappear if the iron content is reduced by less than 1% [47]. $T_V$ is therefore a very good indicator of the quality of the sample. Preparation and analysis were performed in UHV chambers with base pressures of $5\times10^{-10}$ mbar and $5\times10^{-11}$ mbar, respectively. The cleaning cycle began with a 15 h anneal at $(750\pm50)$ °C. It was reported that annealing the sample can lead to the diffusion of intrinsic bulk contaminants to the surface, in particular calcium [39, 48, 49]. These calcium contaminants are suggested to originate from the growth process. To avoid the possibility that calcium or other contaminants were present on the surface the sample was sputtered with $Ar^+$ ions with an energy of 0.5 keV for 1 h. Several studies reported that annealing reduces the oxygen to iron ratio (see e.g. [40, 50, 51]). It was also reported that $Ar^+$ sputtering can reduce this ratio [40, 52]. Therefore, the sample was annealed in an oxygen partial pressure of $2.5\times10^{-6}$ mbar at $(750\pm50)$ °C for 1.5 h. Argon sputtering was performed for 10 min ($I=10\,\mu$A, $E=0.6$ keV) in order to remove any oxide layer which may have formed during annealing in oxygen atmosphere. Sputtering can lead to argon being present on the surface, therefore, sputtering was followed by a flash anneal at $(825\pm50)$ °C. The microscope used in the presented work is a commercial low-temperature slider type STM from Createc. All images presented were obtained in constant current mode at 77 K. STM images were analysed using the Gwyddion package [53]. The STM tips used were polycrystalline tungsten which were electrochemically etched in NaOH.

## III. RESULTS

### A. STM measurements

STM measurements of the $Fe_3O_4(110)$ surface reveal a row reconstruction, which is presented in Fig. 2(a). The rows' ridges run along the $[\bar{1}10]$ direction, which is in accordance with literature [39–45]. The reconstructions periodicity of 25 Å (see Fig. 2(b), top right inset) closely matches three times the lattice parameter of

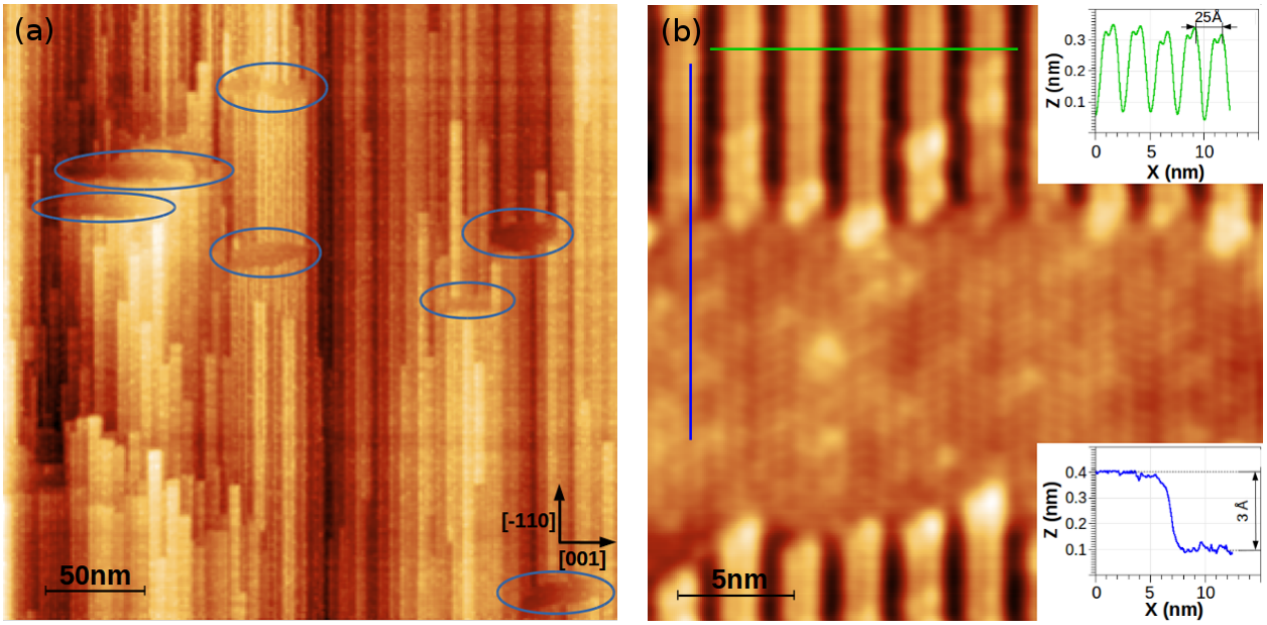


FIG. 2. (a) $(320 \times 320)\,\mathrm{nm}^2$, $V = 1.56\,\mathrm{V}$, $I = 0.12\,\mathrm{nA}$. Row reconstructed structure with the rows' ridges running along the $[\bar{1}10]$ direction. The blue ovals highlight where the rows break, to reveal an atomically flat region. (b) $(29 \times 29)\,\mathrm{nm}^2$, $V = 1.58\,\mathrm{V}$, $I = 0.11\,\mathrm{nA}$. A region highlighted by the blue ovals in (a). Inset top right; line profile corresponding to the green line segment which demonstrates the row periodicity of 25 Å, this periodicity closely matches 3 times the surface unit cell parameter along the [001] direction. Inset bottom right; line profile corresponding to blue line segment illustrating that the two structures are separated vertically by 3 Å, this distance closely matches the distance between consecutive A- or B-planes.

8.396 Å. Along the $[\bar{1}10]$ direction the rows break, revealing an atomically flat surface region, the blue ovals in Fig. 2(a) highlight its occurrence. Fig. 2(b) depicts on a smaller scale this atomically flat surface and the adjacent rows. The dimensions of individual areas of this structure range from (10 - 50) nm along the [001] direction and (1 - 10) nm along the $[\bar{1}10]$ direction.

The area which is revealed when the rows break has always been observed to be below the adjacent rows. The two structures are separated vertically by 3 Å (Fig. 2(b), bottom right inset), which corresponds to the interplanar distance between identical planes, i.e. A-plane to A-plane or B-plane to B-plane. Fig. 3 displays a high-resolution STM image of the atomically flat surface region presented in Fig. 2(b). Features are separated by 6 Å along the $[\bar{1}10]$ lattice direction. Along the [001] direction the distance between features varies periodically between ∼6 Å and ∼11 Å. The average atomic separation of ∼8.5 Å along [001] direction and the 6 Å separation along the $[\bar{1}10]$ lattice direction compare well to the surface unit cell parameters of 8.396 Å and 5.937 Å illustrated in Fig. 1.

Further annealing in a UHV atmosphere leads to the gradual reduction in size and occurrence of the atomically flat surface regions until this reconstruction is no longer present on the surface. We believe that sputtering prior to annealing is pivotal to the existence of the atomically flat regions alongside the row reconstruction. A surface inhabiting both reconstructions can be regained by repeating the 1 h $Ar^+$ sputter and 1.5 h anneal, this is the case whether the surface is annealed in a UHV or oxygen atmosphere post sputter. Further work is required to understand both the relationship between the two vastly different reconstructions and how/if the coverage of the atomically flat surface regions can be increased. The strong influence that the cleaning procedure has on the surface structure is unsurprising. Several TMO sur-

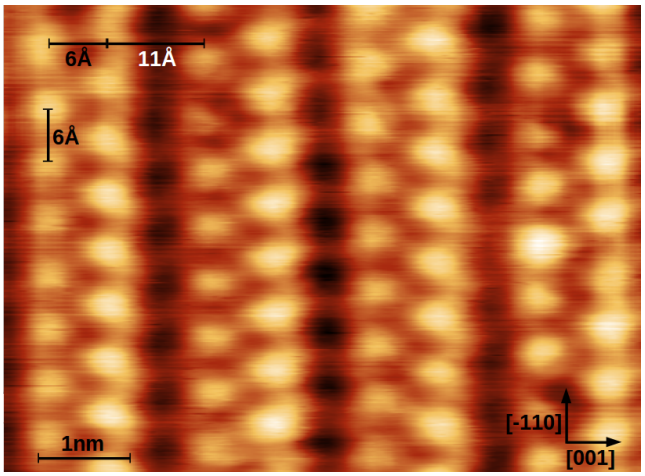


FIG. 3. $(70 \times 50)\,\mathrm{Å}^2$ STM image of the atomically flat surface revealed when the rows break. $V = 0.87\,\mathrm{V}$, $I = 0.07\,\mathrm{nA}$.

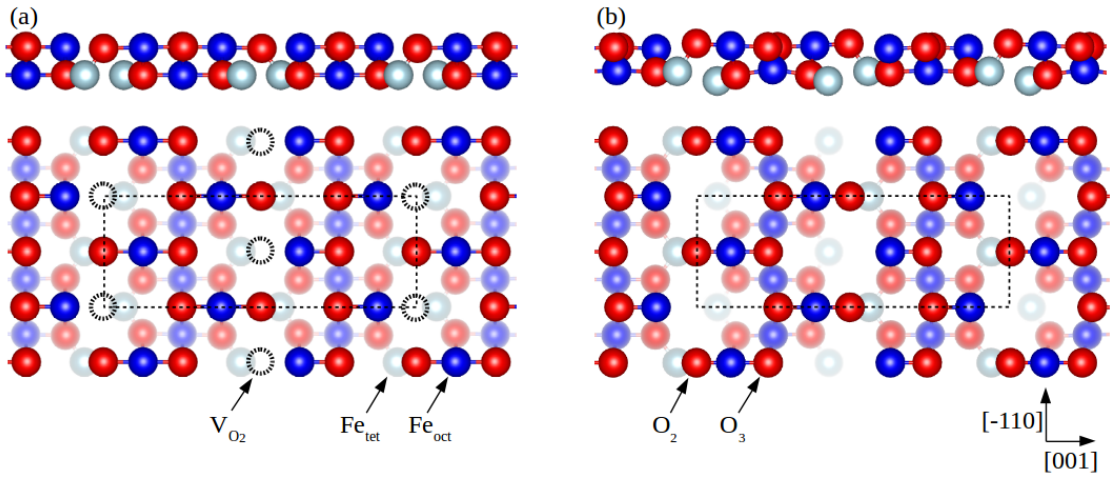


FIG. 4. (a) depicts the side view and top view of the unrelaxed geometry of the B-terminated $(1 \times 2)$ two-fold coordinated oxygen vacancy model. (b) depicts the fully relaxed geometry. Two-fold and three-fold coordinated surface oxygen atoms are indicated. $O_2$ atoms are bonded to one surface $Fe_{oct}$ and one sub-surface $Fe_{tet}$, while $O_3$ atoms are bonded to one surface $Fe_{oct}$ and two sub-surface $Fe_{oct}$. Rows of oxygens running in the $[\bar{1}10]$ direction alternate between $O_2$ and $O_3$. The black dashed circles in (a) highlight the surface $O_2$ vacancies.

faces including magnetite have reported a strong dependence of the surface structure on the cleaning procedure [34, 35, 54] and in particular sputtering [30, 55]. Furthermore, we believe it is possible that minor details such as number of annealing cycles and polishing procedure can influence the ratio between the two surface structures.

### B. DFT+U calculations

First principle calculations were performed in order to gain an understanding of the atomically flat surface revealed when the rows break. Full spin-polarized DFT calculations were performed using the projector-augmented-wave (PAW) method [56] as implemented in the Vienna *Ab-initio* Simulation Package (VASP) [57–59]. The electron exchange and correlation were treated within the generalized gradient approximation (GGA) using the Perdew-Burke-Ernzerhof (PBE) functional [60]. To account for the strong onsite Coulomb interaction of localized electrons, Hubbard U corrections with $U = 4.50\,\text{eV}$ [61] and $J = 0.89\,\text{eV}$ [62] were applied on the Fe atoms. The $Fe_3O_4(110)$ surface was simulated by periodic supercells formed by slabs consisting of 10 unit layers and a 15 Å-wide vacuum. The positions of the atoms in the two layers most distant from the surface were constrained to account for the bulk. The Brillouin zone integrations were performed using a 2×3×1 Monkhorst-Pack (MP) grid [63]. The applied energy cutoff was 500 eV. Each system was relaxed until the Hellmann-Feynman force on each atom was less than $0.05\,\text{eV/Å}$.

A previous DFT study of the (110) surface of magnetite concluded that the oxygen vacated B-plane represents the most energetically stable termination of those considered [64]. It should be noted that B-terminated magnetite contains two inequivalent oxygen atoms. All of which are bonded to one surface $Fe_{oct}$, half are bonded to one sub-surface $Fe_{tet}$ and the other half are bonded to two sub-surface $Fe_{oct}$. Henceforth, these inequivalent surface oxygen atoms on the B-terminated surface will be notated $O_2$ and $O_3$, with the subscript indicating the oxygen atoms coordination number. The aforementioned DFT study [64] examined three-fold oxygen vacan-

| Surface | [001] | [$\bar{1}$10] | [110] | Sub-surface | [001] | [$\bar{1}$10] | [110] |
|---|---|---|---|---|---|---|---|
| $O_2(1)$ | 0.13 | 0.00 | 0.25 | $Fe_{tet}(1)$ | 0.17 | 0.00 | -0.33 |
| $Fe_{oct}(1)$ | -0.17 | 0.00 | 0.07 | O(1) | 0.14 | 0.10 | -0.01 |
| $O_3(1)$ | -0.30 | 0.00 | -0.03 | O(2) | 0.14 | -0.10 | -0.01 |
| $O_3(2)$ | 0.30 | 0.00 | -0.03 | $Fe_{oct}(1)\&(2)$ | 0.00 | 0.00 | 0.28 |
| $Fe_{oct}(2)$ | 0.17 | 0.00 | 0.07 | O(3) | -0.14 | -0.10 | -0.01 |
| $O_2(2)$ | -0.13 | 0.00 | 0.25 | O(4) | -0.14 | 0.10 | -0.01 |
| $Fe_{oct}(3)$ | -0.03 | 0.00 | -0.09 | $Fe_{tet}(2)$ | -0.17 | 0.00 | -0.33 |
| $O_3(3)$ | -0.12 | 0.00 | -0.06 | $Fe_{tet}(3)$ | -0.12 | 0.00 | 0.19 |
| $O_3(4)$ | 0.12 | 0.00 | -0.06 | O(5) | 0.03 | 0.05 | 0.16 |
| $Fe_{oct}(4)$ | 0.03 | 0.00 | -0.09 | O(6) | 0.03 | -0.05 | 0.16 |
| | | | | $Fe_{oct}(3)\&(4)$ | 0.00 | 0.00 | 0.23 |
| | | | | O(7) | -0.03 | -0.05 | 0.16 |
| | | | | O(8) | -0.03 | 0.05 | 0.16 |
| | | | | $Fe_{tet}(4)$ | 0.12 | 0.00 | 0.19 |

TABLE I. Relaxation in Ångström of the surface and sub-surface atoms within the B-terminated $O_2$ surface vacancy model (Fig. 4). Top to bottom corresponds to atoms from left to right in the unit cell depicted in Fig. 4(b). Positive magnitudes in the [001] and $[\bar{1}10]$ directions follow the direction of the vectors in Fig. 4, while a negative [110] magnitude corresponds to a relaxation into the bulk.

cies only. Here, we have considered both of the possible oxygen vacancies on B-terminated $Fe_3O_4(110)$. Initially, $(1 \times 1)$ models which contained one surface oxygen vacancy were considered, the $O_2$ vacancy was found to be energetically favourable. With the features observed in the STM images in mind, $(1 \times 2)$ models which contain two surface oxygen vacancies have been examined. Fig. 4 depicts the $(1 \times 2)$ $O_2$ vacancy model. Every second $O_2$ atom is vacant along the row of $O_2$ atoms, and hence are separated by the $[\bar{1}10]$ unit cell distance, in the adjacent $O_2$ rows the vacancies are shifted by half the unit cell. The $(1 \times 2)$ $O_3$ vacancy model is identical apart from the oxygen vacancies coordination. DFT calculations of these two models indicate, as is the case for $(1 \times 1)$ models, that two-fold coordinated oxygen represents the more energetically stable vacancy, with the difference in surface energy being $54\,\mathrm{meV/\AA^2}$ [65]. Fig. 4(a) and 4(b) depict the initial and relaxed geometry of the B-terminated $O_2$ vacancy model. Furthermore, the magnitude of the surface and sub-surfaces atoms relaxations are listed in Table. 1. To the best of our knowledge the oxygen vacated A-plane has not been investigated. However, anion vacancies on the electron deficient A-plane are likely to give rise to an energetically unfavorable surface termination.

### C. Simulation of STM images

STM images of the $(1 \times 2)$ B-terminated $O_2$ vacancy model have been simulated. Previous studies of the Fe(110) surface [66, 67] and the oxidised Cu(100) surface [68] have demonstrated that the tip can influence the features observed in STM images. The aforementioned study of the oxidised Cu(100) surface determined that an oxygen terminated tip was highly likely. With these points in mind, we have calculated STM images with and without the inclusion of the STM tip. Simulations without the STM tip correspond to the Tersoff-Hamann scheme [69]. Simulations which included the STM tip utilize the revised Chen's derivative rule [70] and are implemented in the BSKAN code [71, 72]. W[111] and W[110] oriented tips which are clean or oxygen terminated have been considered. We feel that comparison between experimental and Tersoff-Hamann simulated STM images provides the best analysis of the proposed model. It should be noted however, that oxygen terminated tips provided similar simulated STM images (not shown here).

Two high resolution STM images are shown in Fig. 5(a) and 5(b), below each of the STM images sit the Tersoff-Hamann simulated STM images of the $(1 \times 2)$ B-terminated $O_2$ vacancy model shown in Fig 4. The simulated images show a good agreement with experiment. The black dashed rectangle in each of the simulated images represents the $(1 \times 2)$ surface unit cell, positioned identically to the surface unit cell depicted in Fig. 4. All of the features within the surface unit cell are positioned above the four surface $Fe_{oct}$ atoms. This is not surprising since the $Fe_{oct}$ 3d level sits at the Fermi level [4, 19] and the oxygen 2p level sits several $eV$ below the Fermi level [4]. Previous studies of the (111) and (001) surfaces of magnetite also interpreted protrusions in constant current STM images as $Fe_{oct}$ atoms [33, 34]. The unit cells in Fig. 5 reveal that the brightest features in each of the simulated images differ. In Fig. 5(c) the two brightest features are positioned above $Fe_{oct}$ atoms which are bonded to two surface oxygen atoms, in contrast, the brightest features in Fig. 5(d) are positioned above $Fe_{oct}$ atoms which are bonded to one surface oxygen atom. This is clearly due to the surface local density of states at different energy ranges.

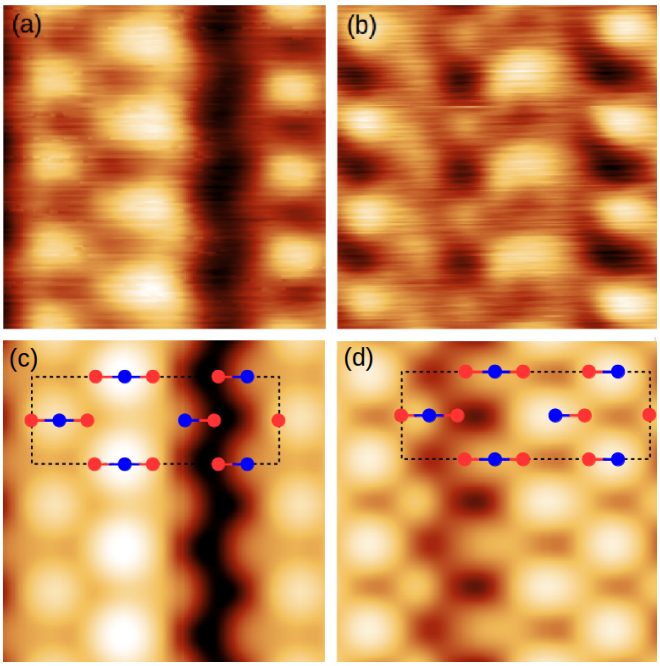


FIG. 5. (a),(b) High resolution $(21 \times 21)\,\mathrm{\AA^2}$ STM images. (a) $V = 0.87\,\mathrm{V}$, $I = 0.07\,\mathrm{nA}$, (b) $V = 0.60\,\mathrm{V}$, $I = 0.78\,\mathrm{nA}$. Simulated STM images calculated at 0.87 V (c) and 0.60 V (d), respectively. The simulated STM images correspond to a Tersoff-Hamann calculation of the $(1 \times 2)$ B-terminated $O_2$ vacancy model. The black dashed rectangle in (c) and (d) corresponds to the surface unit cell of the model, identical to the surface unit cell illustrated in Fig. 4. Blue circles represent iron surface atoms, while red circles represent oxygen surface atoms.

### D. Spin density distributions

Fig 6. illustrates the calculated spin density distributions of the iron atoms in the first four layers of the proposed surface model. Blue and silver spin densities represent the majority and minority spin orientations. $Fe_{oct}$ and $Fe_{tet}$ sites are antiferromagnetically coupled, as is the case for bulk magnetite. A spherical distribution

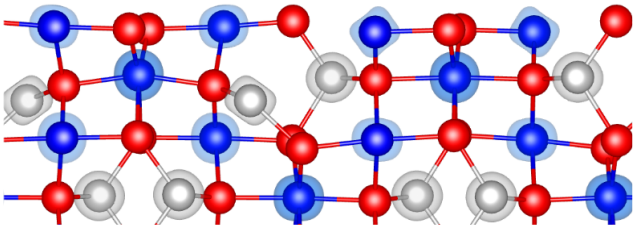

FIG. 6. Side view illustration of the B-terminated $O_2$ vacancy model. Overlayed onto the iron atoms is their respective spin density distributions obtained from DFT calculations. Blue and silver distributions represent the majority and minority spin channels. A spherical spin distribution indicates a half filled d-band , and hence $Fe^{3+}$ character. Any deviation from spherical shape indicates increased $3d^6$ occupation, and hence $Fe^{2+}$ character. Surface $Fe_{oct}$ atoms all display 2+ character, on the other hand sub-surface $Fe_{oct}$ atoms exhibit 3+ character.

indicates a half filled d-band, and hence $Fe^{3+}$ character. Deviation from a spherical distribution indicates an increased occupation of the $3d^6$ orbital, and hence $Fe^{2+}$ character [73]. The four surface $Fe_{oct}$ atoms all display 2+ character. This is in agreement with a previous study of $Fe_3O_4(001)$, which demonstrated a progressive reduction of surface iron to $Fe^{2+}$ as the surface Fe/O ratio was increased [73]. $Fe_{oct}$ atoms in the sub-surface layer all display $Fe^{3+}$ character. $Fe_{tet}$ atoms which have a bond removed due to the existence of surface oxygen vacancies exhibit $Fe^{2+}$ character. The remaining $Fe_{tet}$ atoms display $Fe^{3+}$ character, as is the case for bulk magnetite.

A polar surface can compensate for its polarity by reducing its surface charge to zero [22]. In order to examine how the existence of oxygen vacancies and predicted $Fe_{oct}$ charge ordering influences the stability of this surface we have calculated the surface charge for ionic conditions. Iron atoms are assigned as either $Fe^{2+}$ or $Fe^{3+}$ based on whether their spin density distribution is spherical or not and this charge is distributed evenly amongst its bonds. Two surface oxygens are bonded to two sub-surface $Fe^{3+}_{oct}$(6-fold) and one surface $Fe^{2+}_{oct}$(4-fold), resulting in a charge of $\frac{3}{6}+\frac{3}{6}+\frac{2}{4}=\frac{3}{2}\,e^-$ each. Further two surface oxygens are bonded to two sub-surface $Fe^{3+}_{oct}$(6-fold) and one surface $Fe^{2+}_{oct}$(3-fold), resulting in a charge of $\frac{3}{6}+\frac{3}{6}+\frac{2}{3}=\frac{5}{3}\,e^-$ each. Finally, two surface oxygens are bonded to one sub-surface $Fe^{3+}_{oct}$(4-fold) and one surface $Fe^{2+}_{oct}$(4-fold), resulting in a charge of $\frac{3}{4}+\frac{2}{4}=\frac{5}{4}\,e^-$ each. Therefore, the unit cell has a charge excess of $2(\frac{3}{2})+2(\frac{5}{3})+2(\frac{5}{4})-4(2)=\frac{5}{6}\,e^-$. For comparison, stoichiometric B-terminated magnetite has a charge excess of $3\,e^-$ for the same area if the numbers of electrons per bond is the same as that of the bulk. Increased surface covalent character, out of plane charge transfer or a combination of both can lead to charge neutral and stable surface.

The largest and brightest features in Fig. 3 form rows separated by 17 Å along the [001] direction, the orientation of these features differ from row to row. This indicates that the surface exhibits longer range order than the $(1\times2)$ model in Fig. 4. It is possible minor relaxations along the $[\bar{1}10]$ direction to give rise to these asymmetries. A $(1\times4)$ model, which corresponds to the $(1\times2)$ model depicted in Fig. 4 doubled in the [001] direction, has been allowed to relax. No additional distortions along the $[\bar{1}10]$ direction were observed. In the present work, we do not determine the nature of these subtly features or the size of the unit. However, the good agreement between experimental and simulated STM images of the B-terminated model containing two-fold oxygen vacancies - which have been predicted by DFT calculations to be the most energetically stable surface vacancy of those considered - leads us to strongly suggest that the investigated surface is B-terminated and contains an ordered array of two-fold oxygen vacancies.

## IV. CONCLUSION

Scanning tunneling microscopy images of the (110) surface of single crystalline magnetite revealed two surface regions: the previously reported row structure and a surprising atomically flat surface structure. Density functional theory calculations of the $Fe_3O_4(110)$ surface indicate that two-fold coordinated oxygen represent the most energetically stable oxygen vacancy on the B-terminated (110) magnetite surface. The comparison between simulated and experimental STM images indicates that the atomically flat surface region corresponds to this aforementioned B-terminated surface containing an ordered array of two-fold coordinated oxygen vacancies. DFT calculations of the spin density distributions indicate charge ordering of surface and sub-surface octahedral iron. Charge ordering on this oxygen vacated surface reduces the surface charge, additional polarity compensation mechanisms such as increased surface covalent character and/or charge transfer can lead to a stabilized surface. The determination of the surface structure and specifically the mechanism which stabilises this surface may provide insight into how polar and transition metal oxide surfaces reconstruct. The existence of two drastically different structures on the same surfaces indicates that the surface can be stabilised by more than one mechanism. This observation along with the intricacy of the discussed surface structure highlights the complexity of both magnetite's and transition metal oxide surfaces in general.

## ACKNOWLEDGMENTS

This work was supported by Science Foundation Ireland through the Principal Investigator grant (12/IA/1264). Krisztián Palotás would like to acknowledge a SASPRO Fellowship (1239/02/01) and a Hungarian Eötvös Fellowship (2016-11).


* wallsb@tcd.ie


[1] J. V. Badding, Nat Mater **2**, 208 (2003).
[2] S. Lany, J. Phys.: Condens. Matter **27**, 283203 (2015).
[3] Y. Shimakawa, Y. Kubo, and T. Manako, Nature **379**, 53 (1996).
[4] R. Arras, B. Warot-Fonrose, and L. Calmels, J. Phys.: Condens. Matter **25**, 256002 (2013).
[5] A. Yanase and N. Hamada, J. Phys. Soc. Jpn. **68**, 1607 (1999).
[6] E. J. W. Verwey, Nature **144**, 327 (1939).
[7] J. P. Shepherd, J. W. Koenitzer, R. Aragón, C. J. Sandberg, and J. M. Honig, Phys. Rev. B **31**, 1107 (1985).
[8] F. P. D. Silva and L. M. Rossi, Tetrahedron **70**, 3314 (2014).
[9] G. S. Parkinson, Z. Novotný, P. Jacobson, M. Schmid, and U. Diebold, J. Am. Chem. Soc. **133**, 12650 (2011).
[10] K. T. Rim, D. Eom, S.-W. Chan, M. Flytzani-Stephanopoulos, G. W. Flynn, X.-D. Wen, and E. R. Batista, J. Am. Chem. Soc. **134**, 18979 (2012).
[11] X. Li and J. Paier, J. Phys. Chem. C **120**, 1056 (2016).
[12] E. Wada, K. Watanabe, Y. Shirahata, M. Itoh, M. Yamaguchi, and T. Taniyama, Appl. Phys. Lett. **96**, 102510 (2010).
[13] J. García and G. Subías, J. Phys.: Condens. Matter **16**, R145 (2004).
[14] F. Zhou and G. Ceder, Phys. Rev. B **81**, 205113 (2010).
[15] G. K. Rozenberg, M. P. Pasternak, W. M. Xu, Y. Amiel, M. Hanfland, M. Amboage, R. D. Taylor, and R. Jeanloz, Phys. Rev. Lett. **96**, 045705 (2006).
[16] M. Pasternak, W. Xu, G. Rozenberg, R. Taylor, and R. Jeanloz, J. Magn. Magn. Mater. **265**, L107 (2003).
[17] D. J. Huang, H.-J. Lin, J. Okamoto, K. S. Chao, H.-T. Jeng, G. Y. Guo, C.-H. Hsu, C.-M. Huang, D. C. Ling, W. B. Wu, C. S. Yang, and C. T. Chen, Phys. Rev. Lett. **96**, 096401 (2006).
[18] M. S. Senn, J. P. Wright, and J. P. Attfield, Nature **481**, 173 (2011).
[19] W. Kündig and R. S. Hargrove, Solid State Commun. **7**, 223 (1969).
[20] Z. Zhang and S. Satpathy, Phys. Rev. B **44**, 13319 (1991).
[21] C. Noguera, J. Phys.: Condens. Matter **12**, R367 (2000).
[22] J. Goniakowski, F. Finocchi, and C. Noguera, Rep. Prog. Phys. **71**, 016501 (2007).
[23] A. Barbier, C. Mocuta, and G. Renaud, Phys. Rev. B **62**, 16056 (2000).
[24] O. Dulub, U. Diebold, and G. Kresse, Phys. Rev. Lett. **90**, 016102 (2003).
[25] A. Subramanian, L. D. Marks, O. Warschkow, and D. E. Ellis, Phys. Rev. Lett. **92**, 026101 (2004).
[26] A. Barbier, G. Renaud, and A. Stierle, Surf. Sci **402-404**, 757 (1998).
[27] J. Goniakowski and C. Noguera, Surf. Sci. **365**, L657 (1996).
[28] C. Noguera, A. Pojani, P. Casek, and F. Finocchi, Surf. Sci. **507-510**, 245 (2002).
[29] M. Ritter and W. Weiss, Surf. Sci. **432**, 81 (1999).
[30] J. Moosburger-Will, M. Krispin, M. Klemm, and S. Horn, Surf. Sci. **605**, 1445 (2011).
[31] T. J. Beck, A. Klust, M. Batzill, U. Diebold, C. Di Valentin, and A. Selloni, Phys. Rev. Lett. **93**, 036104 (2004).
[32] O. Dulub, L. A. Boatner, and U. Diebold, Surf. Sci. **519**, 201 (2002).
[33] R. Bliem, E. McDermott, P. Ferstl, M. Setvin, O. Gamba, J. Pavelec, M. A. Schneider, M. Schmid, U. Diebold, P. Blaha, L. Hammer, and G. S. Parkinson, Science **346**, 1215 (2014).
[34] T. K. Shimizu, J. Jung, H. S. Kato, Y. Kim, and M. Kawai, Phys. Rev. B **81**, 235429 (2010).
[35] S. K. Shaikhutdinov, M. Ritter, X.-G. Wang, H. Over, and W. Weiss, Phys. Rev. B **60**, 11062 (1999).
[36] N. Berdunov, S. Murphy, G. Mariotto, and I. V. Shvets, Phys. Rev. B **70**, 085404 (2004).
[37] R. S. Cutting, C. A. Muryn, G. Thornton, and D. J. Vaughan, Geochim. Cosmochim. Acta **70**, 3593 (2006).
[38] J. Noh, O. I. Osman, S. G. Aziz, P. Winget, and J.-L. Brédas, Chem. Mater. **27**, 5856 (2015).
[39] R. Jansen, B. Nelissen, D. Abraham, H. van Kempen, and V. Brabers, IEEE Trans. Magn. **30**, 4506 (1994).
[40] R. Jansen, V. Brabers, and H. van Kempen, Surf. Sci. **328**, 237 (1995).
[41] R. Jansen, J. Vac. Sci. Technol. B **14**, 1173 (1996).
[42] G. Maris, O. Shklyarevskii, L. Jdira, J. Hermsen, and S. Speller, Surf. Sci. **600**, 5084 (2006).
[43] G. Maris, L. Jdira, J. Hermsen, S. Murphy, G. Manai, I. Shvets, and S. Speller, IEEE Trans. Magn. **42**, 2927 (2006).
[44] G. Maris, L. Jdira, J. G. H. Hermsen, S. Murphy, G. Manai, I. V. Shvets, and S. Speller, Jpn. J. Appl. Phys. **45**, 2225 (2006).
[45] G. S. Parkinson, P. Lackner, O. Gamba, S. Maaß, S. Gerhold, M. Riva, R. Bliem, U. Diebold, and M. Schmid, Surf. Sci. **649**, 120 (2016).
[46] K. Fleischer, R. Verre, O. Mauit, R. G. S. Sofin, L. Farrell, C. Byrne, C. M. Smith, J. F. McGilp, and I. V. Shvets, Phys. Rev. B **89**, 195118 (2014).
[47] R. Aragón, R. Rasmussen, J. Shepherd, J. Koenitzer, and J. Honig, J. Magn. Magn. Mater. **54-57**, 1335 (1986).
[48] G. Mariotto, S. Murphy, and I. V. Shvets, Phys. Rev. B **66**, 245426 (2002).
[49] S. Ceballos, G. Mariotto, K. Jordan, S. Murphy, C. Seoighe, and I. Shvets, Surf. Sci. **548**, 106 (2004).
[50] G. Mariotto, S. F. Ceballos, S. Murphy, N. Berdunov, C. Seoighe, and I. V. Shvets, Phys. Rev. B **70**, 035417 (2004).
[51] G. Mariotto, S. Murphy, N. Berov, S. Ceballos, and I. Shvets, Surf. Sci. **564**, 79 (2004).
[52] K. Jordan, A. Cazacu, G. Manai, S. F. Ceballos, S. Murphy, and I. V. Shvets, Phys. Rev. B **74**, 085416 (2006).
[53] D. Nečas and P. Klapetek, Open Phys. **10**, 181 (2012).
[54] U. Diebold, Surf. Sci. Rep. **48**, 53 (2003).
[55] A. R. Lennie, N. G. Condon, F. M. Leibsle, P. W. Murray, G. Thornton, and D. J. Vaughan, Phys. Rev. B **53**, 10244 (1996).
[56] P. E. Blöchl, Phys. Rev. B **50**, 17953 (1994).

[57] G. Kresse and D. Joubert, Phys. Rev. B **59**, 1758 (1999).
[58] G. Kresse and J. Furthmüller, Comput. Mater. Sci. **6**, 15 (1996).
[59] G. Kresse and J. Furthmüller, Phys. Rev. B **54**, 11169 (1996).
[60] J. P. Perdew, K. Burke, and M. Ernzerhof, Phys. Rev. Lett. **77**, 3865 (1996).
[61] V. I. Anisimov, I. S. Elfimov, N. Hamada, and K. Terakura, Phys. Rev. B **54**, 4387 (1996).
[62] V. I. Anisimov, J. Zaanen, and O. K. Andersen, Phys. Rev. B **44**, 943 (1991).
[63] H. J. Monkhorst and J. D. Pack, Phys. Rev. B **13**, 5188 (1976).
[64] Y. Li, K. Yao, and Z. Liu, Surf. Sci. **601**, 876 (2007).
[65] K. Reuter and M. Scheffler, Phy. Rev. B **65**, 035406 (2001).
[66] S. Heinze, S. Blügel, R. Pascal, M. Bode, and R. Wiesendanger, Phys. Rev. B **58**, 16432 (1998).
[67] G. Mándi and K. Palotás, Appl. Surf. Sci. **304**, 65 (2014).
[68] H. Mönig, M. Todorović, M. Z. Baykara, T. C. Schwendemann, L. Rodrigo, E. I. Altman, R. Pérez, and U. D. Schwarz, ACS Nano **7**, 10233 (2013).
[69] J. Tersoff and D. R. Hamann, Phys. Rev. B **31**, 805 (1985).
[70] G. Mándi and K. Palotás, Phys. Rev. B **91**, 165406 (2015).
[71] K. Palotás and W. A. Hofer, J. Phys.: Condens. Matter **17**, 2705 (2005).
[72] W. Hofer, Prog. Surf. Sci. **71**, 147 (2003).
[73] Z. Novotny, N. Mulakaluri, Z. Edes, M. Schmid, R. Pentcheva, U. Diebold, and G. S. Parkinson, Phys. Rev. B **87**, 195410 (2013).